



THE UNIVERSITY *of* EDINBURGH

Edinburgh Research Explorer

Super-resolved Ultrasound Echo Spectra with Simultaneous Localization using Parametric Statistical Estimation

Citation for published version:

Dermitzakis, A, Diamantis, K, Hopgood, J & Sboros, V 2018, 'Super-resolved Ultrasound Echo Spectra with Simultaneous Localization using Parametric Statistical Estimation' IEEE Access. DOI: 10.1109/ACCESS.2018.2807807

Digital Object Identifier (DOI):

[10.1109/ACCESS.2018.2807807](https://doi.org/10.1109/ACCESS.2018.2807807)

Link:

[Link to publication record in Edinburgh Research Explorer](#)

Document Version:

Peer reviewed version

Published In:

IEEE Access

General rights

Copyright for the publications made accessible via the Edinburgh Research Explorer is retained by the author(s) and / or other copyright owners and it is a condition of accessing these publications that users recognise and abide by the legal requirements associated with these rights.

Take down policy

The University of Edinburgh has made every reasonable effort to ensure that Edinburgh Research Explorer content complies with UK legislation. If you believe that the public display of this file breaches copyright please contact openaccess@ed.ac.uk providing details, and we will remove access to the work immediately and investigate your claim.



Super-resolved Ultrasound Echo Spectra with Simultaneous Localization using Parametric Statistical Estimation

Journal:	IEEE Access
Manuscript ID	Draft
Manuscript Type:	Special Section: Soft Computing Techniques for Image Analysis in the Medical Industry – Current trends, Challenges and Solutions
Date Submitted by the Author:	n/a
Complete List of Authors:	Diamantis, Konstantinos; Heriot-Watt University, Dermitzakis, Aris; University of Patras, Department of Medical Physics Hopgood, James; University of Edinburgh, Institute for Digital Communications, School of Engineering Sboros, Vassilis; Heriot-Watt University, Institute of Biological Chemistry, Biophysics and Bioengineering
Keywords:	Ultrasonic imaging, Ultrasonic variables measurement, Statistical analysis, Bayesian methods, Spectral analysis, Nonlinear acoustics
Subject Category Please select at least two subject categories that best reflect the scope of your manuscript:	Biomedical Engineering, Ultrasonics, ferroelectrics, and frequency control, Signal processing, Imaging
Additional Manuscript Keywords:	Bayesian inference, Markov chain Monte Carlo, medical ultrasound, microbubbles, ultrasound contrast imaging

SCHOLARONE™
Manuscripts

Super-resolved Ultrasound Echo Spectra with Simultaneous Localization using Parametric Statistical Estimation

Konstantinos Diamantis, Aris Dermitzakis, James R. Hopgood, *Member, IEEE*, and Vassilis Sboros

Abstract—Ultrasound contrast imaging (UCI) aims to detect flow changes in the vascular bed that can help differentiate normal from diseased tissues thus providing an early screening tool for diagnosis or treatment monitoring. Ultrasound contrast agents (UCAs), used in UCI, are microbubbles (MB) that scatter ultrasound non-linearly. To date the signal processing research has successfully subtracted signals from the linear response of tissue (“linear signals”), but, in general has not provided a sensitive detection that is specific to the UCA signal. This paper develops a method for the temporal and spectral estimation of linear and non-linear ultrasound echo signals. This technique is based on non-parametric methods for coarse estimation, followed by a parametric method within a Bayesian framework for estimation refinement. The results show that the pulse location can be estimated to within ± 3 sample points accuracy for signals consisting of ≈ 80 sample points depending on the signal type, while the frequency content can be estimated to within 0.050 MHz deviations for frequencies in the 1 to 4 MHz range. This parametric spectral estimation achieved a 5-fold improvement in the frequency resolution compared to Fourier-based methods, and revealed previously unresolved frequency information that led to over 80% correct signal classification for linear and non-linear echo signals.

Index Terms—Bayesian inference, Markov chain Monte Carlo, medical ultrasound, microbubbles, ultrasound contrast imaging

I. INTRODUCTION

A large number of human diseases are associated with abnormal vascular networks such as cancer, ischaemia, inflammation and also novel therapeutic interventions such as tissue regeneration. The measurement of perfusion and its quantification has been the subject of intensive research across the spectrum of imaging technologies for decades. However, the real time detection and monitoring of perfusion or microvascular flow currently represents a major clinical and research bottleneck and is essential in the understanding, diagnosis, and therapy monitoring of such diseases. Ultrasound contrast imaging (UCI) uses injections of sub-capillary sized microbubbles (MB) stabilized with a biocompatible shell in

diameters between $1 - 6 \mu\text{m}$, to ensure image contrast from the vascular bed [1]. Suitably, these MBs remain within the vascular bed and have flow kinetics similar to blood cells. This enables the measurement of vascular and microvascular blood flow using modern ultrasound systems [2], [3]. However, this technology has not achieved quantitative status and, compared to magnetic resonance imaging (MRI) and positron emission tomography (PET), UCI has lower sensitivity and reproducibility and it is highly operator dependent [4]–[7].

Historically, the introduction of MBs to diagnostic ultrasound contrast imaging sparked a debate on their physical behaviour and a number of theoretical models have been proposed [8], [9]. This debate remains open and inconclusive [10]. This is partly due to the high number of parameters that affect the behaviour of MBs and the difficulty in isolating these experimentally. As a result this theoretical debate has not converged into models that can aid the UCI signal processing design. State of the art clinical UCI signal processing is based on basic amplitude and phase modulation techniques, that successfully suppress linear tissue echo but offer very little in the enhancement or differentiation of non-linear MB signals [11]–[14]. In addition, despite the introduction in the clinic of a few UCI applications (e.g. liver lesion diagnosis), today the MB signal and image processing remain sub-optimal and there are still significant discrepancies between *in-vitro* and *in-vivo* contrast image data that are difficult to interpret [15]. Thus, signal processing tools especially designed for the analysis of echo signals need to be developed. MBs provide ultrasound echoes [13], [14], that can be distinguished from linear scatters such as tissue; statistical properties of these echo returns include total intensity, spectral content, and temporal information. By detecting the presence of UCAs and differentiating them from tissue, the resolution and sensitivity of ultrasound images can be greatly improved to detect vascular activity.

Compared to soft tissue, MBs are more compressible and expandable when insonified with ultrasound. As a result when exposed to ultrasound they oscillate under the varying pressure of the field. This oscillating behaviour results in high scattering strength of the contrast MBs [16]. In the ultrasound literature, soft tissue provides linear scatter, which will be related to the incident field following linear scatter theory. This means that the linear scatter spectra are expected to consist of specific frequency components, with small variations among them. By contrast, MBs usually provide non-linear scatter and they may generate a more variable spectral content including various sub- and ultra-harmonics [17], [18]. Most traditional

This work was supported by the Science and Technology Facilities Council (STFC-ST/M007804/1). Asterisk indicates corresponding author.

K. Diamantis is with the Institute of Biological Chemistry, Biophysics and Bioengineering (IB3), Heriot-Watt (HW) University, Edinburgh, Scotland, EH14 4AS, UK (e-mail: K.Diamantis@hw.ac.uk).

A. Dermitzakis is with the Biomedical Technology Unit, Department of Medical Physics, University of Patras, Rio, 26504, Greece (e-mail: dermitzak@upatras.gr).

J. R. Hopgood is with the Institute for Digital Communications, School of Engineering, University of Edinburgh, Edinburgh, Scotland, EH9 3JL, UK (e-mail: James.Hopgood@ed.ac.uk).

*V. Sboros is with IB3, HW (e-mail: V.Sboros@hw.ac.uk).

frequency estimation techniques in ultrasonics are based on the Fourier transform (FT) [19]. The frequency resolution (Δf), i.e. the ability to distinguish two frequency components that are closely-spaced, depends solely on the signal length and the sampling frequency. However, the ultrasound signals are short in duration and the FT results in spectral peaks that are not narrow enough to determine their exact position and number. Moreover, the FT does not localize in time whereas in ultrasonics analysis, the pulse locations and durations are also important.

In previous work [20], [21] a Bayesian spectral analysis technique was introduced providing improved frequency resolution compared to the FT for echo signals from non-linear scatterer. Similar results were obtained from a preliminary study on echo signals from linear scatterers [22]. Hence, it is important to investigate whether “hidden” spectral features can be used to identify unclassified scatterer received by a transducer. In this study the frequency estimation system is expanded to include temporal information. This was accomplished by incorporating a modified voice activity detection (VAD) technique, mainly used in speech processing [23]–[25]. From the observation of responses from ultrasound scatterers, the pulse location estimation of the echo signals in ultrasound imaging is similar to the signal burst detection in speech detection. However, if the SNR or the amplitudes are low, the performance of the VAD is poor. There is little information in the ultrasonic literature about joint estimation of pulse locations and frequencies system especially for multiple pulse echo signals from MBs [26]. A first study in [27] showed accurate pulse location for MB echo signals on top of the frequency estimation shown in [21], [22]. The current work builds on the temporal and spectral analysis tools first presented in [21], [27], by proposing a lower-uncertainty spectral estimator through statistical post-processing of the system’s output, and by providing an evaluation of the system performance. The latter was accomplished by testing the system on both synthetic data, and experimentally *in-vitro*, with linear scatterer and non-linear MB ultrasound signals. The findings are discussed with a view to further development of the algorithm as well as to precision improvements in the ultrasound signal characterization.

II. MATERIALS AND METHODS

A. Single Ultrasound Scatter Experiment

A commercial phased array ultrasound transducer (S3, Philips, Andover, MA, USA) was used to acquire echo signals from solid copper spheres (Goodfellow Cambridge Ltd, Huntingdon, UK) and Definity MBs (Lantheus Inc, MA, USA). The solid copper spheres (SCSs) were used as linear scatterers [11], [28]. All the measurements were carried out using a modified ultrasound scanner (Sonos5500 Philips Medical Systems, Andover, MA, USA). The transmit focus was set to 60 mm depth and the acquisitions were performed between 70 mm and 80 mm depths for both SCSs and MBs, to ensure that the same calibrated settings applied. At this depth range, peak negative pressure of 550 kPa was recorded, ensuring MB survival for more than 50% of the MBs. A 6-cycle sinusoid

was used as the excitation pulse with a transmit frequency (f_0) equal to 1.62 MHz. The transducer was not operated at its resonance (around 2.8 MHz), but rather at the low edge of its bandwidth. Data were sampled at 20 MHz and the raw echo signals were stored for further processing. A schematic diagram of the experimental setup, consisting of a water tank and tubing that allowed the flow of SCSs or MBs, is shown in Fig. 1.

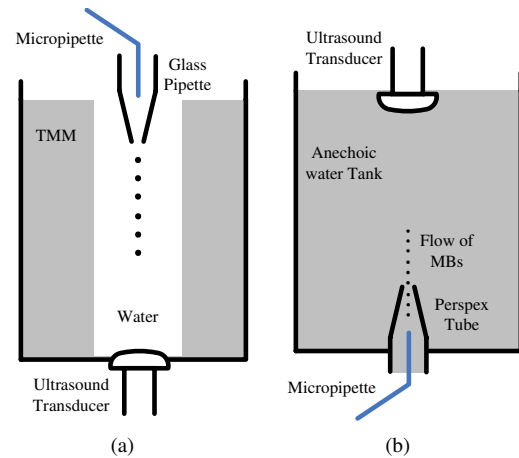


Fig. 1. Illustration of the experimental setup for echo signal acquisition from (a) SCSs, and (b) MBs.

In Fig. 1(a), a water tank was used to measure the SCS scatterer. This setup was previously used to calibrate the ultrasound receiver at a point in the field in order to provide absolute calibration of microbubble signals [28]. A 4 cm diameter hole at the base of the tank was sealed with a 25 μm thickness Mylar film to provide an acoustic window. The central cylindrical space defined by the circular acoustic window at the base is filled with degassed water. The remainder of the tank was filled with the tissue mimicking material (TMM) [29], in order to minimize multiple reflections. A glass pipette was placed at the top of the tank and its bottom tip with 1 mm internal diameter was held at the center of the tank. Alignment was achieved by aligning a thread inserted through the glass pipette, which was held straight by attaching a lead bead to the bottom. The maximum echo from the thread ensured alignment of the SCS path with the centre of the ultrasound beam. SCSs with a variety of radii, ranging from 29 μm to 58 μm , were dropped individually into the glass pipette, with the help of another micro-pipette, and then into the tank following a path that coincided with the centre of the ultrasound transducer.

The setup for MB echo acquisition (Fig. 1(b)) was similar but with an inverted geometry. The tank was filled with degassed water. A Perspex tube was placed at the center of the bottom of the tank with an 8 mm internal diameter. The tip of a glass micropipette, with approximate diameter 100 μm , was placed at the center of the Perspex tube. The suspension of MBs was diluted enough to ensure the release of single MBs at the tip of the micropipette. The flow in the Perspex tube ensured a MB path at the centre of the ultrasound beam and towards the face of an ultrasound probe, which was placed at the top of the tank.

B. Non-parametric Temporal and Spectral Estimation

Pulse location and spectral estimates using conventional non-parametric estimation (NPE) methods were initially employed to provide the initial conditions for the proposed parametric estimation system. For the pulse localization the Hilbert transform (HT) is commonly used in ultrasound imaging [30] as it enables the extraction of the envelope of the modulated signal [19]. A wavelet denoising (WD) method [31], [32] was also adopted as it presents various advantages compared to traditional filtering approaches in cases of multiple-pulse signals [31], [32]. The combination of the above 2 methods (HTWD) improves the pulse detection accuracy but may fail when there are closely-spaced pulses present in the measured echo signals. The latter was resolved with the addition of a VAD complement [23], [25], and the formation of a joint HTWD-VAD method as presented in [27]. For the spectral estimation, the multi-taper spectrum [33] was chosen to initially analyse the ultrasound signals in the frequency domain [21]. In this technique, several data windows are used on the same data record to obtain a number of modified periodograms, which are averaged to produce a multi-taper spectrum. By reducing the variance, a cleaner spectrum is achieved compared to the Discrete Fourier Transform (DFT).

C. Estimation Refinement

1) *Parametric Modelling*: For the experimentally measured echoes from MBs and SCSs, the number of pulse segments in the signal and the number of frequency components in each pulse segment were all unknown. Based on the excitation pulse used, the multiple pulse-echo signals can be modelled as several segments of sum of sinusoids in noise [34]. It was assumed that there were m pulses in the observed signal with N data points. For each pulse, there are 2 change-points, T_i and T_{i+1} , hence $2m$ change-points in total. A typical MB signal with 9 pulse segments and 2900 points is shown in Fig. 2. The multiple pulses model can be defined as follows:

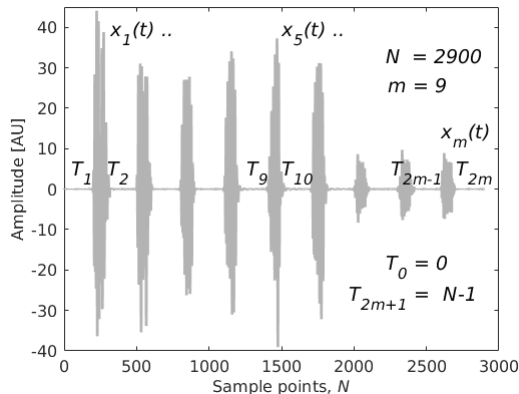


Fig. 2. Display of an experimental MB raw signal including 9 MB responses in the time domain as recorded after array processing.

$$D_0 : x(t) = n(t)$$

$$D_{k_m} : x(t) = \begin{cases} n(t) & \text{if } T_{2i-2} \leq t \leq T_{2i-1} - 1, \\ x_i(t) + n(t) & \text{if } T_{2i-1} \leq t \leq T_{2i} - 1, \\ n(t) & \text{if } T_{2m} \leq t \leq T_{2m+1}, \end{cases}$$

where $i \in (1, m)$, and $x_i(t)$ is given by:

$$x_i(t) = \sum_{j=1}^{k_i} a_{c_j, k_i} \cos(\omega_{j, k_i} t) + a_{s_j, k_i} \sin(\omega_{j, k_i} t). \quad (1)$$

Note that the model D_0 corresponds to the lack of any pulses in the observation sequence, and D_{k_m} denotes there are m pulse segments in the signal. The indices k_1, k_2, \dots, k_m denote the number of super-positioned frequency components in the m pulse segments. In each i -th pulse segment, a_{c_j, k_i} and a_{s_j, k_i} are the cosine and sine amplitudes respectively of the ω_{j, k_i} , that is the j -th frequency component of the i -th segment with k_i frequency components. Moreover, $n(t)$ is a sequence of a zero mean white Gaussian noise with variance $\sigma_{k_i}^2$. The signal model can be written in vector-matrix form:

$$\mathbf{x} = \mathbf{G}(\omega_{k_m}, T_{2m}) \mathbf{a}_{k_m} + \mathbf{n}, \quad (2)$$

where $\mathbf{a}_{k_m} \triangleq [\mathbf{a}_{k_1}, \mathbf{a}_{k_2}, \dots, \mathbf{a}_{k_m}]^T$, in which $\mathbf{a}_{k_i} (i = 1, \dots, m) \triangleq [(a_{c_1, k_i}, a_{s_1, k_i}), \dots, (a_{c_{k_i}, k_i}, a_{s_{k_i}, k_i})]^T$ represents the amplitudes of the frequency components in each pulse segment. $\mathbf{G}(\omega_{k_m}, T_{2m})$ is a matrix of non-overlapping elements with a size of $2N \times \sum_{i=1}^m k_i$ given by:

$$\mathbf{G} = \begin{bmatrix} 0 & 0 & \dots & 0 \\ \mathbf{G}_1 & 0 & \dots & 0 \\ 0 & 0 & \dots & 0 \\ 0 & \mathbf{G}_2 & \dots & 0 \\ 0 & 0 & \dots & 0 \\ \vdots & \vdots & \ddots & \vdots \\ 0 & 0 & \dots & 0 \\ 0 & 0 & \dots & \mathbf{G}_m \\ 0 & 0 & \dots & 0 \end{bmatrix}.$$

The matrix \mathbf{G} contains the information about change-points $[T_1, T_2, \dots, T_{2m}]$, and spectral contents $[\omega_{k_1}, \omega_{k_2}, \dots, \omega_{k_m}]$ for m different pulse segments. Each component $\mathbf{G}_i (i = 1, \dots, m)$ in the \mathbf{G} matrix represents a single pulse where the number of frequency components, the frequency values, their amplitudes, and the noise variance are all unknown parameters. They can all be represented by $\theta_{k_i} \triangleq (\omega_{k_i}, \mathbf{a}_{k_i}, \sigma_{k_i}^2)$. As far as each segment is concerned, the \mathbf{G}_i matrix can be defined as:

$$\mathbf{G}_i = \begin{bmatrix} E(\omega_{k_1}, T_{2i-1}) & \dots & E(\omega_{k_i}, T_{2i-1}) \\ E(\omega_{k_1}, T_{2i-1} + 1) & \dots & E(\omega_{k_i}, T_{2i-1} + 1) \\ \vdots & \vdots & \vdots \\ E(\omega_{k_1}, T_{2i} - 1) & \dots & E(\omega_{k_i}, T_{2i} - 1) \end{bmatrix}$$

where $E(\cdot) \triangleq [\cos(\cdot), \sin(\cdot)]$. Moreover, T_{2i-1} and T_{2i} are the two corresponding change-points for each pulse segment.

2) *Joint Posterior Distribution*: The Bayesian posterior probability for the frequencies of a signal provides an accurate estimation of frequency peaks [35]. According to Bayesian inference, samples from the posterior distribution can be drawn given the appropriate prior distributions. These priors reflect the degree of belief of the relevant values of the parameters. The joint prior distribution can be considered as the product of the independent parameter priors, displayed in Table I for the m segments.

TABLE I
PRIOR DISTRIBUTIONS FOR INDEPENDENT PARAMETERS

Parameters	Prior Distributions
T_{2m}	Uniform Distribution
k_m	Truncated Poisson Distribution
ω_{k_m}	Uniform Distribution
\mathbf{a}_{k_m}	Multivariate Normal Distribution
σ_k^2	Jeffrey's uninformative prior
δ_m^2	Inverse Gamma Distribution
Λ_m	Gamma Distribution

In Table I, Λ_m is the hyperparameter of the number of frequency components k_m , and δ_m^2 is the hyperparameter of the amplitudes \mathbf{a}_{k_m} . The joint prior distribution can be expressed in (3):

$$\begin{aligned}
 p(\{k, \theta_k\}_m, T_{2m}) &= p(\{k, \mathbf{a}_k, \omega_k\}_m | \sigma_k^2) p(\sigma_k^2) p(T_{2m}) \\
 &\propto \left(\frac{\Lambda_m^{k_m}}{k_m!} \exp(-\Lambda_m) \times \frac{1}{|2\pi\sigma_k^2 \Sigma_{k_m}|^{1/2}} \times \frac{1}{\pi^{k_m}} \right. \\
 &\quad \times \exp\left[-\frac{\mathbf{a}_{k_m}^T \Sigma_{k_m}^{-1} \mathbf{a}_{k_m}}{2\sigma_k^2}\right] \Big) \\
 &\quad \times \frac{1}{\sigma_k^2} \left(\frac{1}{N-1} \frac{1}{N-2} \cdots \frac{1}{N-2m} \right), \quad (3)
 \end{aligned}$$

where $\Sigma_{k_m}^{-1} = \delta_m^{-2} \mathbf{G}^T(\omega_{k_m}, T_{2m}) \mathbf{G}(\omega_{k_m}, T_{2m})$.

The posterior distribution is the product of the joint prior distribution and the likelihood function, which based on the signal model is given by:

$$\begin{aligned}
 p(\mathbf{x} | \{k, \theta_k\}_m, T_{2m}) &= (2\pi\sigma_k^2)^{-N/2} \times \\
 &\quad \exp\left\{-\frac{1}{2\sigma_k^2} \|\mathbf{x} - \mathbf{G}(\omega_{k_m}, T_{2m}) \mathbf{a}_{k_m}\|^2\right\}, \quad (4)
 \end{aligned}$$

where m in $\{k, \theta_k\}_m$ represents different pulse segments and $\|A\|^2 \triangleq A^T \cdot A$. The posterior distribution in (5) can be obtained after integrating out the nuisance parameters: amplitudes \mathbf{a}_k and noise variance σ_k^2 based on Bayes's rule.

$$\begin{aligned}
 p(T_{2m}, \{k, \omega_k\}_m | \mathbf{x}) &\propto (\gamma_0 + \mathbf{x}^T \mathbf{P}_{k_m} \mathbf{x})^{-(N+v_0)/2} \\
 &\quad \times \frac{(\Lambda_m / [(\delta_m^2 + 1)\pi])^{k_m}}{k_m!} \quad (5)
 \end{aligned}$$

where $\mathbf{P}_{k_m} = \mathbf{I}_N - \mathbf{G}(\omega_{k_m}, T_{2m}) \mathbf{M}_{k_m} \mathbf{G}^T(\omega_{k_m}, T_{2m})$, \mathbf{I}_N is the identity matrix with N -by- N dimensions, and $\mathbf{M}_{k_m}^{-1} = \mathbf{G}^T(\omega_{k_m}, T_{2m}) \mathbf{G}(\omega_{k_m}, T_{2m}) + \Sigma_{k_m}^{-1}$.

3) *Reversible Jump Markov Chain Monte Carlo Algorithm*: The refinement of the model parameters, for both pulse locations and frequency components, using a parametric model with numerical Bayesian method, consisted of two steps in

each iteration. First, based on the initial guesses given by aforementioned combination algorithm of the VAD and the HTWD for envelope detection, a random walk perturbation was adopted as the proposal distribution for refinement of the pulse location estimates. Specifically, the update of each change-point depended on its previous value and performed a local exploration of the initial guess, which can be described as:

$$T^* | T \sim \mathcal{N}(T, \sigma_T^2). \quad (6)$$

where T and T^* are previous state and new state of the change-point respectively. $\mathcal{N}(\cdot)$ represents the normal distribution with mean T and variance σ_T^2 .

Second, for the frequency estimation, a reversible jump Markov chain Monte Carlo (rjMCMC) algorithm was used to explore the regions around dominant peaks from the multitaper power spectrum initial guess. After the pulse locations were coarsely estimated, frequency estimation was performed for different pulse segments. Although the posterior distribution was simplified, it was still highly non-linear, which means the closed form of $p(T_{2m}, \{k, \omega_k\}_m | \mathbf{x})$ can not be easily obtained. Therefore, the rjMCMC algorithm was introduced to sample from the complicated joint posterior distribution and then to estimate the multiple pulse locations and frequency contents for each pulse segment simultaneously. An ergodic Markov chain whose equilibrium distribution is the specific joint posterior distribution given by (5) was formulated. The simulation was run long enough to reach the stationary distribution. The reversible jump technique (rjMCMC) allowed to jump between subspaces of different model orders. Based on the obtained samples, the Maximum A Posterior (MAP) estimator was adopted to obtain a mode of the estimated posterior distribution $\hat{p}(k_m | \mathbf{x})$ and $\hat{p}(\omega_{k_m} | k_m, \mathbf{x})$. Then, the desired parameters (k_m, ω_{k_m}) were estimated as:

$$\begin{aligned}
 \hat{k}_m | \mathbf{x} &= \arg \max_{k_m} \hat{p}(k_m | \mathbf{x}) \\
 \hat{\omega}_{k_m} | \hat{k}_m, \mathbf{x} &= \arg \max_{\omega_{k_m}} \hat{p}(\omega_{k_m} | k_m, \mathbf{x}) \quad (7)
 \end{aligned}$$

For each of the m segments, there are three candidate moves to be selected. The *birth* and *death* moves introduce dimension changes according to the state of Markov chain, by randomly proposing a new frequency on $(0, \pi)$, or randomly removing an existing one respectively. The *update* move only refines the frequencies within the same dimension. Details of the birth, death and update moves can be found in [21].

D. Data Analysis

The Bayesian analysis resulted in a highly multi-modal posterior distribution. This made the interpretation of the algorithm's output difficult and several non-sensible parameter estimates were obtained. Imposing limitations such as $k \leq 20$ in [21] is a partial solution to this problem but higher performance could be achieved if further processing is applied to the rjMCMC frequency estimates. Here, this was accomplished by extracting a reasonable summary of the posterior distribution through clustering and outlier rejection.

An initial processing of a number of synthetic signals using the parametric statistical estimation (PSE) system, enabled comparisons with true pulse locations and frequency components that were known, as well as with estimates derived from non-parametric methods. The algorithm was then set to a large number of realizations ($N_{real} = 500$) when applied to real ultrasound signals, to ensure that there were sufficient data for analysis, since many estimates were ignored during a single-case study. A single realization was also set to a high number of iterations ($N_{iter} = 10000$) to ensure that convergence to a specific model order was achieved. The output data from all realizations were considered for the current processing. They were clustered based on the number of detected frequencies (or else model order, k), so that the marginal posterior distributions of parameters of interest can be considered unimodal. Previous allocation of estimated values in histograms, regardless of the model order [21], was no longer adopted. In this work, realizations with the same number of estimated parameters were grouped in terms of model order and the data from the most frequent model order were chosen for further processing. These enabled the calculation of the mean frequency values and the associated standard deviation by applying normal distribution fits to the data from all the realizations of this model order. Frequency estimates referring to the same frequency component (i.e. the first or the last) may contain values that differ greatly from realization to realization. For this reason all values significantly higher than two times the standard deviation were removed.

The pulse location estimation as well as the frequency estimation based on the post-processing described above were followed for an ultrasound transmit pulse, the MB signal of Fig. 2 containing 9 MB pulses, and also 9 SCS individual responses for comparison. The underlying hypothesis here was that super-resolved spectra are possible to extract using this methodology and that real short duration signals provide a reproducible super-resolved spectrum. Ultrasound linear scatter has a well-defined spectrum and was used here to provide this test. The frequency estimates from the transmit pulse were used as a standard of comparison for all the linear and non-linear ultrasound responses. The frequency estimates from all the MB and the SCS responses were then analysed in an attempt to classify any given response into one of the two categories. Specific features in common for most SCS or MB responses revealed initially by the PSE, and subsequently by the use of data-fitting functions were exploited in order to create N_d data points that render the classification possible. A standard k -means algorithm was employed to solve this clustering problem [36]. The number of clusters (N_{cl}) was 2 and therefore two centroids (c) were eventually estimated. Each data point belonging to either a SCS or MB response was associated to the nearest centroid. The S function is a measure of the distance of all data points from their centroids and is given by:

$$S = \sum_{p=1}^{N_{cl}} \sum_{q=1}^{N_d} \| d_q^{(p)} - c_p \|^2, \quad (8)$$

where $\| d_q^{(p)} - c_p \|^2$ is the Euclidean distance between a data

point $d_q^{(p)}$ and the centroid c_p . The algorithm was repeated several times until the centroids no longer change and the squared error function (S) was minimized.

III. RESULTS: ESTIMATION ALGORITHM

A. Estimation of Synthetic Signals

A synthetic signal was used for an initial performance evaluation of the estimation algorithm. The signal included two pulse segments and consisted of 1500 sample points. As an exemplar, white Gaussian noise with an SNR = 5 dB was also added to the signals. The sampling frequency, f_s , was 20 MHz, and the two pulse segments were synthesized as a sum of 2 and 3 frequency components respectively. The two pulses were located between samples (450, 600) and (750, 850) with frequency components (in MHz) at ($0.6\pi = 1.885$, $0.7\pi = 2.199$) and ($0.2\pi = 0.628$, $0.3\pi = 0.943$, $0.32\pi = 1.005$) respectively. The estimation procedure was repeated for 100 times with different noise realizations, amplitudes, and phase components. An example of such a synthetic signal is shown in Fig. 3(a). The 2nd segment was shorter than the first (100 sample points instead of 150). Given the f_s , all Fourier-based methods result in a Δf comparable to 20 MHz/100 = 0.200 MHz [37]. As a consequence, the two larger frequencies separated by 0.062 MHz were regarded as a single frequency by non-parametric analysis (Fig. 3(b)).

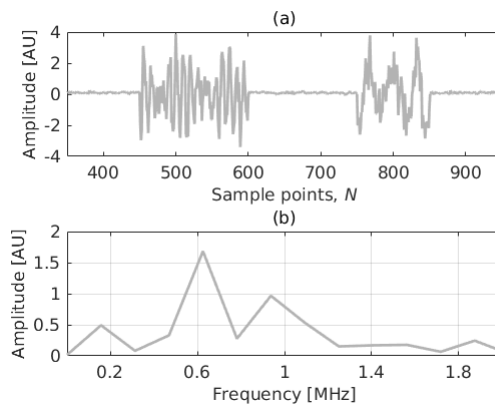


Fig. 3. (a) Display of a synthetic signal consisting of two pulse segments. (b) Fast Fourier Transform (FFT) of the 2nd segment.

The pulse locations from both NPE and PSE are compared in Table II. The NPE resulted in less-accurate average estimates for the starting points of both pulses (1st and 3rd change-points), where a 10 point standard deviation (SD) from the true values was measured. By using the parametric method the accuracy of the pulse location estimates improved significantly with standard deviations no higher than 2 sample points, for both pulses, between the different signals. The results confirmed the higher accuracy of the parametric estimation in cases of lower SNRs. Fig. 4 shows the pulse location convergence diagnostics for the 2nd pulse (3rd and 4th change-points) of a single synthetic signal and thus single algorithm realization, as an example. The pulse location estimates were in this case 750 and 849 for the 3rd and 4th change-point respectively (Fig. 4). The first value (750) was observed with

probability of ≈ 0.5 , clearly standing out from other estimates (≈ 0.2 at best). The second value (849) was observed with a probability of ≈ 0.42 while the probability of the second most frequent estimate (850) was also relatively high (0.34). Both estimates were within the range described in Table II. After the first 1000 iterations, all the change-points, related to the start and end points of pulses, reached their stationary distributions.

TABLE II
NPE AND PSE (MEAN \pm SD IN SAMPLE POINTS) OF PULSE LOCATIONS FOR 100 SYNTHETIC SIGNALS OF VARYING NOISE, AMPLITUDE AND PHASE

Change-point	Ground truth	NPE	PSE
1 st	450	460 \pm 1	452 \pm 2
2 nd	600	602 \pm 4	600 \pm 0

(a) Change-points comparison for the 1st pulse segment

Change-point	Ground truth	NPE	PSE
3 rd	750	760 \pm 2	749 \pm 1
4 th	850	850 \pm 1	850 \pm 1

(b) Change-points comparison for the 2nd pulse segment

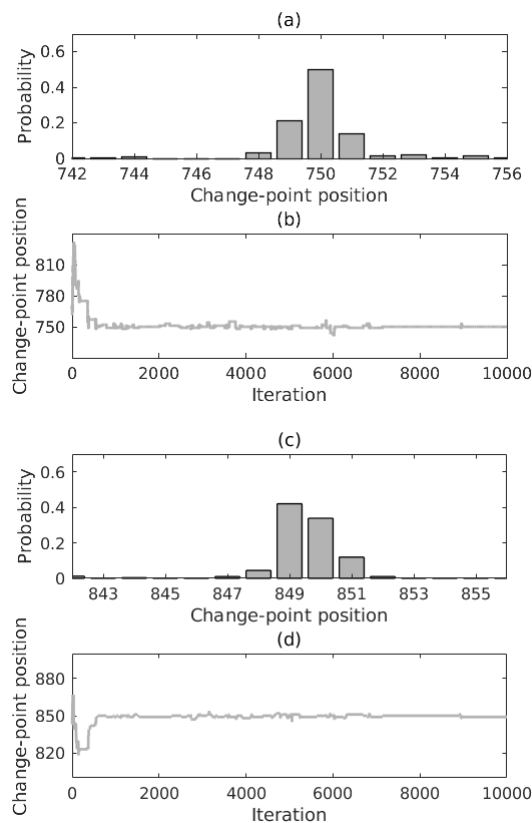


Fig. 4. Localization of the second pulse segment of a single synthetic signal. Histogram of position and convergence diagnostics are shown in (a) and (b) for the 3rd change-point, and in (c) and (d) for the 4th change-point respectively.

Each rjMCMC realization detected a specific number of frequencies for each pulse segment as shown in Fig. 5. For the 1st segment, the most frequent number of frequencies was 2 and for the 2nd segment, the most common value is 3. The detection of the 3rd component indicates the robustness of the new algorithm. Similar to the pulse locations, the frequency

values obtained from 100 realizations using the PSE for the two pulse segments of the synthetic signal were compared to the ground truth, and to the results using NPE (Table III). Both the non-parametric and the parametric methods provided accurate frequency estimates, for the first pulse segment as shown in Table III(a). However, the SD values were almost two orders of magnitude lower for the parametric method compared to the non-parametric one. In Table III(b) for the second pulse segment, the NPE can identify two frequency components where the 2nd was estimated between the 2nd and the 3rd true frequency values. On the other hand, not only did the PSE provide estimates closer to the true values, but it was also able to distinguish the two closely-spaced frequencies.

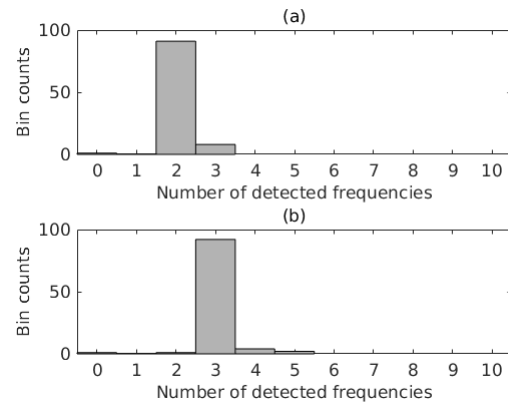


Fig. 5. Histogram showing the number of detected frequencies using a synthetic signal with 100 randomly selected noise, amplitude, and phase components for (a) the first and (b) the second pulse segment. A single rjMCMC realization was performed on the synthetic signal with a random component set, thus 100 rjMCMC realizations in total.

TABLE III
FFT PEAKS AND PSE (MEAN \pm SD IN MHZ) FOR A SYNTHETIC SIGNAL OF 100 RANDOMLY SELECTED NOISE, AMPLITUDE AND PHASE COMPONENTS

Freqs.	Ground truth	FFT peaks	PSE
1 st	2.199	2.200 \pm 0.036	2.199 \pm < 0.001
2 nd	1.885	1.887 \pm 0.053	1.885 \pm 0.001

(a) Frequency estimates comparison for the 1st pulse segment

Freqs.	Ground truth	FFT peaks	PSE
1 st	0.628	0.620 \pm 0.210	0.629 \pm < 0.001
2 nd	0.943	0.979 \pm 0.220	0.939 \pm 0.001
3 rd	1.005	0.0	1.003 \pm 0.001

(b) Frequency estimates comparison for the 2nd pulse segment

Fig. 6 shows the histogram of detected frequencies and the convergence diagnostics for the 2nd pulse of a single realization, as an example. The most frequent value (3) was observed with probability of 0.78, with significant difference from number 4 which was the second most common estimate with a probability of 0.16. It can be seen that the number of detected frequencies converged to the number 3 after about 2000 iterations. As a result of this convergence, the first 2000 iterations can be considered as the burn-in period.

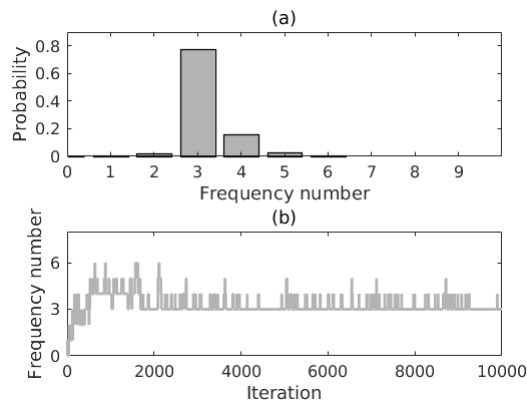


Fig. 6. (a) Histogram of detected frequencies and (b) convergence diagnostics for the 2nd pulse segment of a single synthetic signal, from a single rjMCMC realization.

B. Estimation of an Ultrasound Transmit Pulse

Fig. 7(a) displays an ultrasound transmit pulse (Tx). The pulse had a duration of $\approx 4 \mu\text{s}$ which translated to ≈ 80 sample points, given the f_s used here. This resulted in a Δf comparable to $20 \text{ MHz}/80 = 0.250 \text{ MHz}$ when using non-parametric methods for spectral estimation. The proposed estimation system was applied 500 times to the signal. The two change-points, as estimated using the parametric pulse localization system are also shown in Fig. 7(a) together with their standard deviations. The start of the pulse was located at sample point 24 ± 1 (or $1.2 \mu\text{s}$) and the end at sample point 96 ± 1 (or $4.9 \mu\text{s}$). Importantly a single start and a single end point were found at sample points 30 (or $1.5 \mu\text{s}$) and 120 (or $6.1 \mu\text{s}$) respectively, using the non-parametric estimation. These were not a good estimate of the pulse edges as displayed in Fig. 7(a). Each of the 500 rjMCMC realizations provided detections of specific number of frequencies for the transmit pulse as shown in Fig. 7(b). The most probable number of frequencies (model order) was $k = 10$, which accounted for 76.4% of the realizations, while the number 11 for 20%. The frequency estimates from the rjMCMC realizations that resulted in $k = 10$ were further processed using histograms. These frequency distribution histograms are displayed in Fig. 7(c), together with their normal distribution fits from where it was possible to calculate mean frequency values and their corresponding standard deviations. The result is shown in Table IV and also overlaid to the FFT in Fig. 7(d). Given the Δf limitation, the FFT did not result in more than 6 peaks. The transmit pulse broadly looks like a windowed pure sinusoid, and therefore by Fourier analysis side-lobes are expected. Since there is uncertainty in the start and end of the pulse, some of (but not all) the additional frequencies in Fig. 7(c) effectively represent frequencies in these side-lobes, although these components will have small corresponding amplitudes.

Table IV shows that instead of a single fundamental frequency at 1.62 MHz, which was the f_0 used here, the PSE returned two components around the f_0 . A clean single sinusoidal signature was not expected due to the extreme f_0 used

TABLE IV
PSE FOR AN ULTRASOUND TRANSMIT PULSE (MEAN \pm SD IN MHz)

Frequencies	Transmit pulse
1 st	0.998 ± 0.027
2 nd	1.167 ± 0.031
3 rd	1.562 ± 0.024
4 th	1.717 ± 0.026
5 th	2.070 ± 0.030
6 th	2.264 ± 0.028
7 th	2.602 ± 0.030
8 th	2.850 ± 0.033
9 th	3.211 ± 0.028
10 th	3.297 ± 0.041

here as described in subsection II-A. These two components were $f_1 = 1.562 (\pm 0.024) \text{ MHz}$ and $f_2 = 1.717 (\pm 0.026) \text{ MHz}$ and their corresponding harmonics ($h_x \approx 2 \times f_x$, where $x = 1, 2$) were the last two frequencies of the spectrum, $h_1 = 3.211 (\pm 0.028) \text{ MHz}$ and $h_2 = 3.297 (\pm 0.041) \text{ MHz}$ respectively. These two frequency pairs ($f_1 - f_2$, $h_1 - h_2$) and others from the Table IV (i.e. 5th and 6th) were separated by less than 0.250 MHz, and thus they were not resolved by NPE. By using the rjMCMC algorithm and the processing described in subsection II-D, the Δf was reduced to 0.086 MHz which was the distance between the most closely spaced estimated frequencies (9th and 10th). Further, it is seen from Table IV that SD values were kept below 0.041 MHz at all cases.

C. Estimation of SCS Responses

Fig. 8(a) displays an example of a typical SCS response. This entire signal, received by the ultrasound transducer, consisted of ≈ 1500 sample points and included a single pulse segment of ≈ 80 sample points (or $\approx 4 \mu\text{s}$ duration), similar to the transmit pulse. The two change-points, as estimated using the parametric pulse localization system are also shown in Fig. 8(a), together with their standard deviations. The start of the pulse was located at sample point 580 ± 2 (or $29 \mu\text{s}$) and the end at sample point 655 ± 3 (or $32.75 \mu\text{s}$). The SD values were slightly increased in the SCS signal (up to 3 sample points) compared to the transmit pulse localization (1 sample point). The equivalent start and end points using the NPE were found at sample points 590 (or $29.5 \mu\text{s}$) and 660 (or $33 \mu\text{s}$) respectively (Fig. 8(a)). Each of the 500 rjMCMC realizations provided the detections of a specific number of frequencies as shown in Fig. 8(b). The most probable number of frequencies (model order) was $k = 10$, which accounted for 69.2% of the realizations, while the number 11 accounted for 25.2%. All frequency estimates from the rjMCMC realizations that resulted in $k = 10$ are displayed in the histograms of Fig. 8(c), together with their normal distribution fits. Fig. 8(d) displays the resulting mean frequency and standard deviation values alongside the FFT of the SCS response. The latter as in the transmit pulse case, did not reveal more than 6 peaks. The frequency estimates of Fig. 8(d) using the PSE are shown in Table V (SCS1), where the equivalent estimates of the other 8 SCS responses can also be found.

Table V shows that the PSE resulted in between 9 and 11 frequency components for all SCS responses, which is

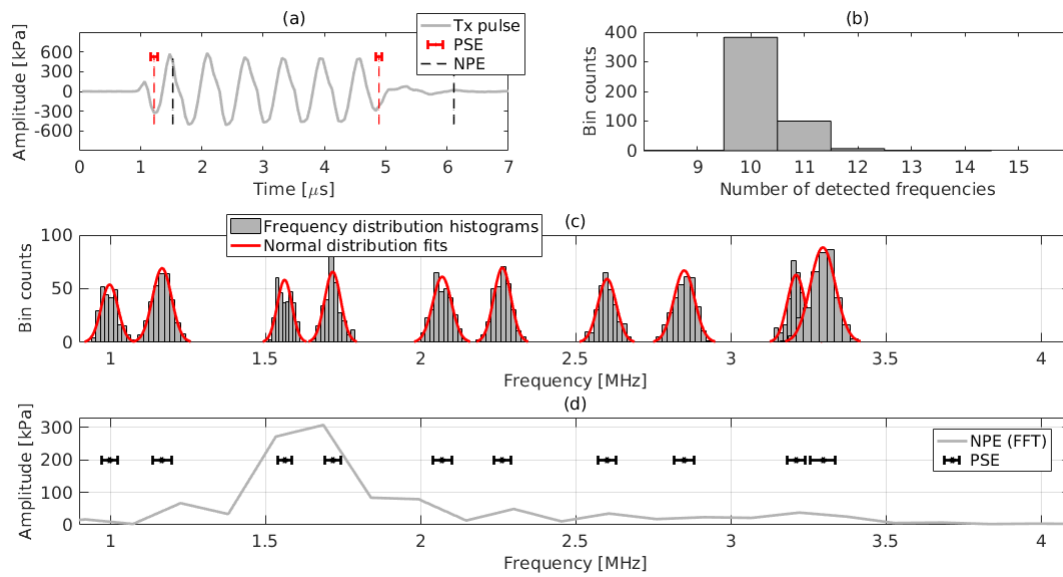


Fig. 7. (a) Display of a 6-cycle ultrasound transmit pulse in the time domain. The pulse locations found by using the PSE system, as well as by the NPE are also indicated. (b) Histogram showing the number of detected frequencies, and (c) frequency distribution histograms and their normal distribution fits using 500 rjMCMC realizations. (d) FFT of the transmit pulse and mean frequency estimates with their standard deviation obtained by the PSE system.

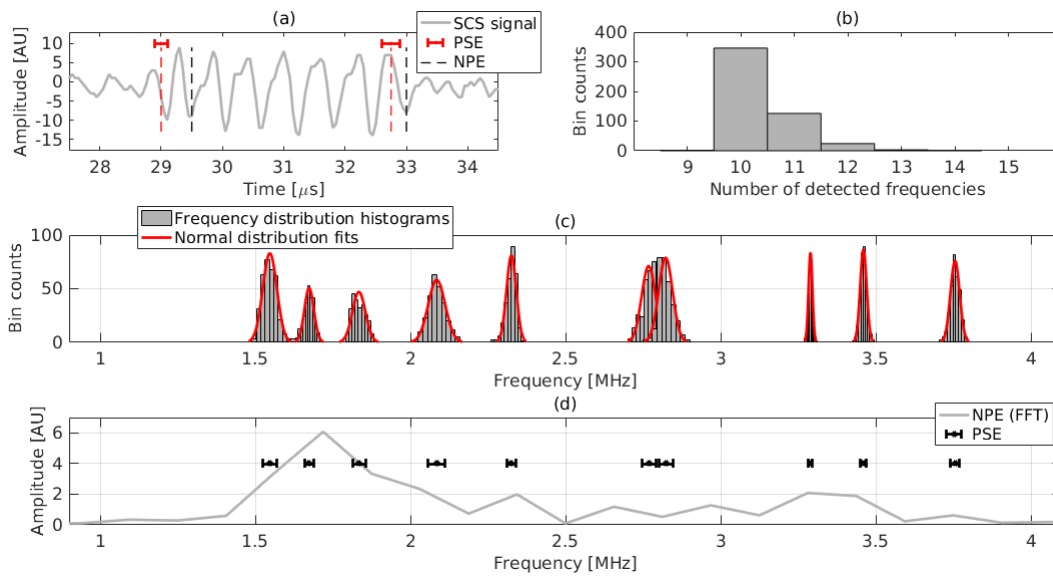


Fig. 8. (a) Display of an experimental SCS response in the time domain. The pulse locations found by using the PSE system, as well as by the NPE are also indicated. (b) Histogram showing the number of detected frequencies, and (c) frequency distribution histograms and their normal distribution fits using 500 rjMCMC realizations. (d) FFT of the SCS signal and mean frequency estimates with their standard deviation obtained by the PSE system.

TABLE V
PSE FOR 9 SCS RESPONSES (MEAN \pm SD IN MHz)

Freqs	SCS1	SCS2	SCS3	SCS4	SCS5	SCS6	SCS7	SCS8	SCS9
1 st	1.547 \pm 0.023	1.253 \pm 0.006	1.307 \pm 0.043	1.391 \pm 0.064	1.379 \pm 0.098	1.364 \pm 0.106	1.205 \pm 0.011	1.619 \pm 0.056	1.554 \pm 0.147
2 nd	1.674 \pm 0.015	1.558 \pm 0.012	1.506 \pm 0.022	1.512 \pm 0.038	1.590 \pm 0.039	1.602 \pm 0.044	1.610 \pm 0.007	1.715 \pm 0.063	1.694 \pm 0.077
3 rd	1.834 \pm 0.021	1.757 \pm 0.015	1.740 \pm 0.017	1.751 \pm 0.022	1.779 \pm 0.029	1.781 \pm 0.031	1.817 \pm 0.032	1.772 \pm 0.090	1.893 \pm 0.047
4 th	2.085 \pm 0.027	2.005 \pm 0.029	2.106 \pm 0.063	2.148 \pm 0.056	2.051 \pm 0.072	2.046 \pm 0.077	2.011 \pm 0.049	1.977 \pm 0.147	1.986 \pm 0.098
5 th	2.326 \pm 0.016	2.165 \pm 0.055	2.306 \pm 0.051	2.273 \pm 0.048	2.212 \pm 0.083	2.258 \pm 0.092	2.423 \pm 0.065	2.304 \pm 0.155	2.361 \pm 0.081
6 th	2.768 \pm 0.023	2.366 \pm 0.023	2.583 \pm 0.078	2.658 \pm 0.074	2.396 \pm 0.076	2.433 \pm 0.078	2.588 \pm 0.060	2.447 \pm 0.111	2.653 \pm 0.077
7 th	2.823 \pm 0.023	2.607 \pm 0.051	2.684 \pm 0.081	2.919 \pm 0.055	2.599 \pm 0.096	2.658 \pm 0.071	2.921 \pm 0.027	2.790 \pm 0.094	2.888 \pm 0.080
8 th	3.290 \pm 0.006	2.884 \pm 0.047	2.959 \pm 0.067	3.227 \pm 0.031	2.935 \pm 0.074	2.887 \pm 0.048	3.261 \pm 0.007	2.967 \pm 0.120	3.255 \pm 0.051
9 th	3.460 \pm 0.011	3.276 \pm 0.021	3.260 \pm 0.013	3.415 \pm 0.013	3.271 \pm 0.025	3.271 \pm 0.014	3.423 \pm 0.006	3.301 \pm 0.039	3.308 \pm 0.046
10 th	3.756 \pm 0.015	3.463 \pm 0.022	3.458 \pm 0.026		3.447 \pm 0.020	3.450 \pm 0.014	3.756 \pm 0.015	3.470 \pm 0.033	3.496 \pm 0.035
11 th		3.759 \pm 0.017	3.683 \pm 0.021		3.719 \pm 0.016	3.729 \pm 0.013		3.754 \pm 0.024	3.635 \pm 0.074

comparable to the number found in the transmit pulse. These results show that the SCS responses were reproducible and that 9 responses are an adequate sample size to describe their distribution. The fundamental frequency values found were consistently similar to those of the transmit pulse. Specifically, the PSE returned a single frequency component between 1.506 MHz (SCS3) and 1.619 MHz (SCS8), for all SCS responses. The mean and SD values of these components were 1.566 ± 0.041 MHz. Thus, $4 \times \text{SD}$ (i.e. 95% of the distribution) corresponded to 10.6% of the mean value. This result is statistically similar to the f_1 (1.562 MHz) of the transmit pulse (subsection III-B). The frequency component closest to the f_2 of the transmit pulse ranged between 1.674 MHz (SCS1) and 1.817 MHz (SCS7) for all SCS responses. The mean and SD values of these components were 1.752 ± 0.044 MHz, with $4 \times \text{SD}$ corresponding to 10.2% of the calculated mean value. This result is not significantly different to the f_2 (1.717 MHz) of the transmit pulse (subsection III-B).

High reproducibility was found for the two harmonic frequency components, which were approximately in the $2 \times f_x$ range. First, all SCS responses included strictly one frequency component in the narrow range between 3.227 MHz (SCS4) and 3.301 MHz (SCS8). Their mean and SD values were 3.268 ± 0.021 MHz, with $4 \times \text{SD}$ corresponding to 2.6% of the calculated mean value. Second, a single frequency component for each SCS response was found in the also narrow range between 3.415 MHz (SCS4) and 3.496 MHz (SCS9). Their mean and SD values were 3.454 ± 0.024 MHz, with $4 \times \text{SD}$ corresponding to 2.8% of the calculated mean value. The two components in these ranges represented a shift to larger values compared to the harmonics h_1 (3.211 MHz) and h_2 (3.297 MHz) of the transmit pulse. Importantly, Table V shows that only two frequency components per SCS response were found in the harmonic frequency range, with the exception of SCS9 that resulted in 3. In addition, the SCS8 response included a second spectral signature in the f_2 range. Frequency pairs corresponding to $f_1 - f_2$ (average difference 0.185 ± 0.039 MHz), and $h_1 - h_2$ (average difference 0.186 ± 0.024 MHz) were separated by less than 0.250 MHz, and were therefore resolved only after using the PSE. The minimum Δf measured was 0.053 MHz that was the distance between the 8th and the 9th frequency estimates of the SCS9 response. Table V also shows that several frequencies between 2 MHz and 3 MHz were in common for only a group of 3–4 of the SCS responses, and were not repeated in all of them. Further, it is seen that SD values varied from a few kHz to 0.155 MHz. However the larger SD values were associated mainly with the SCS8 response, and the average SD value was 0.049 MHz.

D. Estimation of MB Responses

The enlarged version for a single pulse segment of Fig. 2, is illustrated in Fig. 9(a) for clarity. This was similar in duration to the transmit pulse or the SCS response shown above (≈ 80 sample points or $\approx 4 \mu\text{s}$), resulting in the same conventional $\Delta f = 0.250$ MHz. The proposed PSE system was applied 500 times to the MB signal and the results for

the segment are shown in Fig. 9. The two change-points, as estimated using the parametric pulse localization system are also shown in Fig. 9(a), together with their standard deviations. The start of the pulse was located at sample point 305 ± 5 (or $15.5 \mu\text{s}$) and the end at sample point 379 ± 10 (or $19.3 \mu\text{s}$). The SD values were significantly higher (up to 10 sample points) compared to the SCS pulse localization (3 sample points at worst). The equivalent start and end points using the NPE were found at sample points 310 (or $15.8 \mu\text{s}$) and 380 (or $19.4 \mu\text{s}$) respectively (Fig. 9(a)). Fig. 9(b) displays the number of detected frequencies for the single MB pulse of Fig. 9(a) and for the 500 rjMCMC realizations. The most probable number of frequencies (model order) was $k = 14$, which accounted for 49% of the realizations, while the number 15 accounted for 36%, and the number 16 for 10%. Similar to the previous subsection, all frequency estimates from the rjMCMC realizations for $k = 14$ were further processed. The frequency distribution histograms are displayed in Fig. 9(c), together with their normal distribution fits from where it was possible to calculate mean frequency values and their corresponding standard deviations. Fig. 9(d) displays the resulting mean frequency and standard deviation values alongside the FFT of the MB response. The latter did not reveal more than 7 peaks. The frequency estimates of Fig. 9(d) using the PSE are shown in Table VI (MB2), where the equivalent estimates of the other 8 MB responses can also be found.

The results from all the different MBs showed that there was reproducibility on these individual frequency signatures but the spread of responses was wider compared to the SCS, and often there was significant overlap between the significant fundamental and harmonic frequencies. Table VI shows that the PSE resulted in between 8 and 15 frequency components for the 9 MB pulses. This is a much wider range compared to that of the SCS responses. Particularly, the MB responses resulted in a higher number of > 3 MHz frequencies compared to the SCS ones, which made the harmonic frequency definition less straightforward. For the MB2 response, the equivalent to the f_1 frequency was $1.567 (\pm 0.028)$ MHz and its harmonic was $h_1 = 3.221 (\pm 0.032)$ MHz. However, f_2 was not distinct, since the 4th frequency estimate significantly overlapped with the 5th (Fig. 9(c)). Therefore, it was not clear whether f_2 was $1.686 (\pm 0.029)$ MHz or $1.756 (\pm 0.047)$ MHz. The corresponding harmonic h_2 , was also not distinct and both the 12th and the 13th frequencies of the spectrum were candidates. In such cases, the fundamental component (f_x) closest to the transmit one was considered for further analysis. Subsequently, those frequency components closest to 2 times the selected f_x were assumed to be their corresponding harmonics (h_1, h_2). The same processing was followed for all MB responses.

The PSE returned one frequency component between 1.556 MHz (MB1) and 1.654 MHz (MB5), for all MB responses. The mean and SD values of these components were 1.603 ± 0.038 MHz. Thus, $4 \times \text{SD}$ (i.e. 95% of the distribution) corresponded to 9.4% of the mean value. This result is not significantly different to the frequency f_1 (1.562 MHz) of the transmit pulse (subsection III-B). The frequency component closest to the f_2 (1.717 MHz) of the

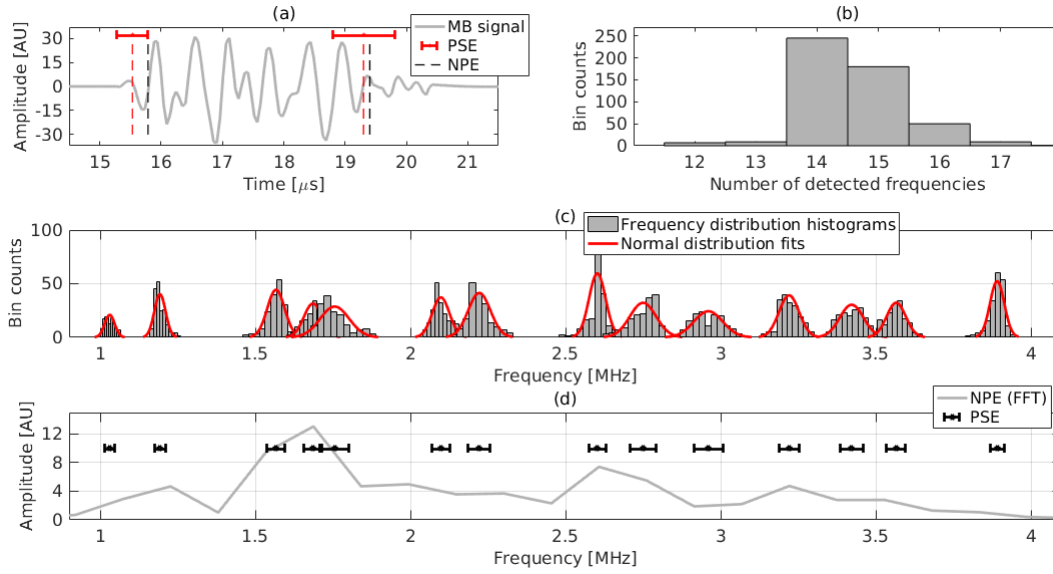


Fig. 9. (a) Individual display of the second MB response from Fig. 2 in the time domain. The pulse locations found by using the PSE system, as well as by the NPE are also indicated. (b) Histogram showing the number of detected frequencies and (c) frequency distribution histograms and their normal distribution fits using 500 rjMCMC realizations. (d) FFT of the MB response and mean frequency estimates with their standard deviation obtained by the PSE system.

TABLE VI
PSE FOR 9 MB RESPONSES (MEAN \pm SD IN MHz)

Freqs.	MB1	MB2	MB3	MB4	MB5	MB6	MB7	MB8	MB9
1 st	0.983 \pm 0.021	1.031 \pm 0.016	1.127 \pm 0.018	1.309 \pm 0.048	1.027 \pm 0.027	1.266 \pm 0.024	1.583 \pm 0.020	1.603 \pm 0.018	1.562 \pm 0.024
2 nd	1.147 \pm 0.035	1.193 \pm 0.018	1.476 \pm 0.030	1.425 \pm 0.026	1.246 \pm 0.035	1.473 \pm 0.029	1.704 \pm 0.028	1.700 \pm 0.029	1.723 \pm 0.023
3 rd	1.287 \pm 0.061	1.567 \pm 0.028	1.623 \pm 0.027	1.634 \pm 0.031	1.453 \pm 0.036	1.645 \pm 0.037	2.098 \pm 0.039	2.193 \pm 0.040	2.116 \pm 0.035
4 th	1.556 \pm 0.030	1.686 \pm 0.029	1.788 \pm 0.045	1.754 \pm 0.055	1.654 \pm 0.034	1.724 \pm 0.068	2.579 \pm 0.060	2.262 \pm 0.044	2.468 \pm 0.040
5 th	1.685 \pm 0.040	1.756 \pm 0.047	2.013 \pm 0.043	1.963 \pm 0.063	1.783 \pm 0.054	1.961 \pm 0.057	2.645 \pm 0.046	2.364 \pm 0.044	2.824 \pm 0.089
6 th	1.816 \pm 0.076	2.098 \pm 0.028	2.188 \pm 0.046	2.248 \pm 0.090	2.010 \pm 0.056	2.147 \pm 0.110	2.729 \pm 0.047	2.853 \pm 0.043	2.957 \pm 0.092
7 th	2.131 \pm 0.052	2.222 \pm 0.036	2.451 \pm 0.080	2.419 \pm 0.046	2.192 \pm 0.063	2.494 \pm 0.097	3.170 \pm 0.036	3.164 \pm 0.098	3.196 \pm 0.051
8 th	2.274 \pm 0.104	2.603 \pm 0.027	2.692 \pm 0.035	2.684 \pm 0.046	2.437 \pm 0.068	2.744 \pm 0.094	3.340 \pm 0.033	3.239 \pm 0.060	3.252 \pm 0.025
9 th	2.553 \pm 0.105	2.750 \pm 0.042	2.834 \pm 0.044	2.939 \pm 0.039	2.626 \pm 0.093	3.008 \pm 0.042	3.496 \pm 0.059	3.361 \pm 0.035	3.353 \pm 0.034
10 th	2.818 \pm 0.040	2.960 \pm 0.047	3.023 \pm 0.037	3.093 \pm 0.027	2.964 \pm 0.073	3.141 \pm 0.031	3.714 \pm 0.034	3.476 \pm 0.057	
11 th	2.934 \pm 0.056	3.221 \pm 0.032	3.227 \pm 0.027	3.208 \pm 0.042	3.094 \pm 0.042	3.386 \pm 0.062			
12 th	3.186 \pm 0.047	3.422 \pm 0.038	3.473 \pm 0.017	3.588 \pm 0.016	3.265 \pm 0.041	3.528 \pm 0.034			
13 th	3.366 \pm 0.035	3.566 \pm 0.031		3.863 \pm 0.012	3.444 \pm 0.066	3.882 \pm 0.026			
14 th	3.570 \pm 0.026	3.891 \pm 0.023			3.648 \pm 0.050				
15 th	3.873 \pm 0.022				3.921 \pm 0.025				

transmit pulse was between 1.685 MHz (MB1) and 1.788 MHz (MB3). The mean and SD values of these components were 1.727 ± 0.039 MHz, with $4 \times \text{SD}$ corresponding to 9% of the calculated mean value. The harmonic frequency components that corresponded to $\approx 2 \times f_1$, ranged between 3.141 MHz (MB6) and 3.265 MHz (MB5). Their mean and SD values were 3.206 ± 0.038 MHz, with $4 \times \text{SD}$ corresponding to 4.6% of the calculated mean value. This result is not significantly different to the h_1 (3.211 MHz) of the transmit pulse (subsection III-B). Likewise, the harmonic frequency components that corresponded to the $\approx 2 \times f_2$, ranged between 3.366 MHz (MB1) and 3.648 MHz (MB5). Their mean and SD values were 3.468 ± 0.100 MHz, with $4 \times \text{SD}$ corresponding to 11.6% of the calculated mean value. This result indicates a shift to larger values compared to the h_2 (3.297 MHz) of the transmit pulse. Note, that in the f_2 , h_1 , and h_2 ranges there were several MB responses that provided more than one frequency components, thus showing a larger variability compared to the SCS responses. Similar to the SCS spectra, there were

several frequencies from the Table VI separated by less than 0.250 MHz, and were therefore resolved only after using the PSE. The minimum Δf was found to be 0.056 MHz which was the distance between the 7th and the 8th frequency estimates from the results of the MB9 pulse. Importantly Δf was similar to that found in subsection III-C, which demonstrates the consistency of the algorithm. Table VI also shows that there were a number of frequencies between 2 MHz and 3 MHz, that did not reveal a particular trend between the resulting frequency values of the MB responses. Further, it is seen from Table VI that all SD values were kept below 0.147 MHz, and the average SD value was 0.045 MHz.

IV. RESULTS: DATA CLASSIFICATION

A. Classification Features

All resulting frequency estimates were put into two separate cumulative histograms one for the SCS and one for the MB responses, with a 0.020 MHz bin width. The two histograms are shown together in Fig. 10. The PSE of the

SCS responses showed that most echoes from linear scatterers included specific frequency components, forming relatively high and narrow histogram peaks in the frequency ranges primarily between 3 MHz and 3.8 MHz and secondarily between 1.5 MHz and 1.8 MHz. This is related to the fact that in each of the two fundamental and two harmonic signatures there was only one frequency value found, apart from two cases mentioned in subsection III-C. By contrast, the MB frequency values in Fig. 10 were more spread across the bandwidth. There were several less pronounced peaks, that were shorter and broader compared to the SCS population, which reflected the larger variability and overlap in frequency values across the MB responses. These histograms show frequency distribution patterns that may help differentiate the two populations.

Kernel smoothing functions were employed to fit the data around the 5 most significant spectral peaks of the two histograms [38]. Such functions perform better than normal distribution fits with continuously distributed samples as these shown in Fig. 10. They were used here to confirm the equivalent f_1, f_2, h_1, h_2 frequency components that were obtained from the individual analysis of the SCS and MB responses in subsections III-C and III-D respectively, without taking into account the transmit pulse frequency estimates. This is closer to a real imaging setting, where the knowledge of the transmit pulse is not provided. The mean frequency estimates and their standard deviations derived by the smoothing functions, are shown in Table VII. The first 4 frequency estimates in Table VII for the SCS responses, compare well to the mean values calculated in subsection III-C, from Table V. The first 3 frequency estimates in Table VII for the MB responses, are also not significantly different from the mean values calculated in subsection III-D, from Table VI. Only the 4th frequency estimate (3.585 ± 0.060 MHz) is significantly different from the value calculated in subsection III-D (3.468 ± 0.100 MHz). By visual inspection, the latter value correlates to a lower and wider histogram peak (Fig. 10) between the two peaks which provided the 3rd and 4th mean frequency values in Table VII for the MB responses. This is an extra indicator of the larger variability across the MB population compared to the SCS one.

TABLE VII
FIVE HIGHEST PEAKS (MEAN \pm SD IN MHz) FROM THE CUMULATIVE
FREQUENCY DISTRIBUTION HISTOGRAMS INCLUDING ALL THE rjMCMC
REALIZATIONS FOR ALL SCS AND MB RESPONSES

Frequencies	SCS	Frequencies	MB
1 st	1.573 ± 0.056	1 st	1.586 ± 0.037
2 nd	1.751 ± 0.029	2 nd	1.705 ± 0.044
3 rd	3.264 ± 0.021	3 rd	3.194 ± 0.092
4 th	3.457 ± 0.025	4 th	3.585 ± 0.060
5 th	3.737 ± 0.027	5 th	3.872 ± 0.027

B. SCS and MB Differentiation

Mixed plots are shown in Fig. 11 in an attempt to distinguish the MB from the SCS responses and classify any of the 18 given signals as either linear or non-linear scatter. The plots aim to exploit the different frequency values and respective uncertainties found in the SCS and MB populations as described above. In Fig. 11(a) the f_1 frequency was plotted over

the $h_2 - h_1$ difference resulting in a concentration of 8 out of 9 SCS data points in a narrow-band area (between 0.15-0.2 MHz) in the centre of the graph. In Fig. 11(b) the f_1 frequency was plotted over the h_1 frequency with the SCS data points concentrated on the centre-top area of the graph. This is a diagonal band for the SCS signals, while the MB population was less clearly defined. However the SCS and MB populations were not fully differentiated, as shown by the errorbar overlap. In Fig. 11(c), the h_1 frequency was plotted over the h_2 frequency resulting in the concentration of most SCS data points in a narrow centre-right region.

Fig. 12 is a similar comparison to that of Fig. 11 including the output from all rjMCMC realizations instead of average values, which enabled classification using a standard k -means clustering method. In Fig. 12(a), the two centroids were calculated to (1.566, 0.181) MHz and (1.609, 0.374) MHz for the SCS and the MB data respectively. The centroids fitted well with the values displayed in Table VII and resulted in 90.1% correct classification for any given input signal. Similarly, Fig. 12(b) is the equivalent to Fig. 11(b) and includes the signal classification information. The two centroids were calculated to (1.568, 3.268) MHz and (1.604, 3.166) MHz for the SCS and the MB data respectively, and the percentage of correct signal classification is 82.8%. Finally, Fig. 12(c) corresponded to Fig. 11(c). In this case, the two centroids were calculated to (3.256, 3.441) MHz and (3.189, 3.566) MHz for the SCS and the MB data respectively, and the percentage of correct signal classification was 88.2%.

V. DISCUSSION

The spectral estimation of ultrasound scatter signals can be achieved with high accuracy using parametric methods. Closely spaced frequencies 0.053 MHz apart can be resolved, while the signal duration does not allow less than 0.250 MHz separation for any non-parametric method. These figures are approximately a 5-fold improvement in frequency resolution (Δf). For the example signals examined here, this resulted in double the amount of detected frequencies compared to Fourier Transform based methods. The parametric spectral estimation was particularly efficient in detecting frequencies with low amplitudes in the FFT spectrum, such as all components > 3 MHz in Figs. 7(c), 8(c) and 9(c) (harmonic content). The frequency estimates were also associated with low standard deviations (SD) always below 0.150 MHz and ≈ 0.050 MHz on average, for frequency values in the MHz range. These SD values are up to 5 times lower compared to these reported in [21]. The improvement is due to the post-processing which uses a larger number of rjMCMC realizations and separates the frequency estimates based on the model order of each realization (subsection II-D). Such low SD values resulted in revealing: (a) the similarity of the SCS and MB signals with that of the transmit signal in the pair of fundamental frequency components, (b) the fundamental and harmonic components reproducibility across the population of the 9 SCS signals, which also suggests that 9 signals is an adequate sample size for the SCS population in order to characterize its spectral content. These results confirm the linearity of the SCS which had different sizes.

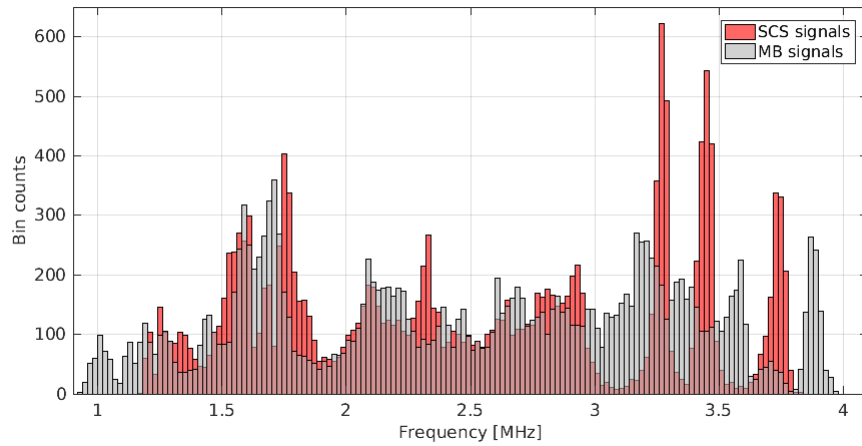


Fig. 10. Cumulative frequency distribution histograms from 9 MB and 9 SCS responses respectively, using 500 rjMCMC realizations. The bin width was set to 0.020 MHz.

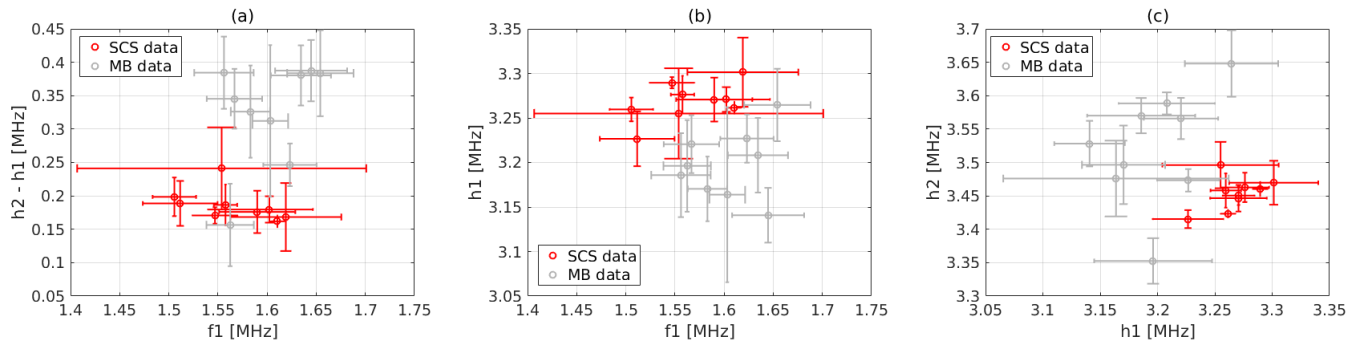


Fig. 11. Plots for SCS and MB differentiation using various combinations of mean frequency values and their standard deviations obtained by the parametric spectral estimation. (a) The f_1 is plotted over the $h_2 - h_1$ difference based on the frequency estimates of the 9 SCS and the 9 MB responses. (b) The f_1 is plotted over the h_1 and (c) the h_1 is plotted over the h_2 .

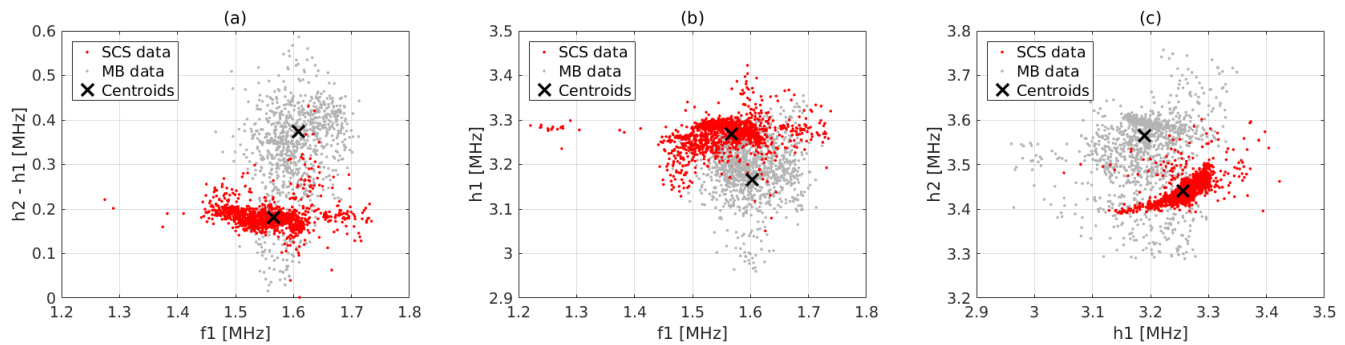


Fig. 12. Scatter plots and k -means clustering using frequency estimates from all rjMCMC realizations, for the 9 SCS and the 9 MB responses. (a) The f_1 is plotted over the $h_2 - h_1$ difference resulting in 90.1% correct signal classification. (b) The f_1 is plotted over the h_1 and (c) the h_1 is plotted over the h_2 with 82.8% and 88.2% correct signal classification respectively.

In addition to the automatic spectral estimation, the proposed system allows the simultaneous accurate localization of each pulse. This is expected as it is inherent to the function of the algorithm, i.e. a specific number of frequencies is expected within the bounds of one signal, which helps differentiate with accuracy the time domain of the signal from that of the surrounding noise. This is not the case for non-parametric methods that provide several miscalculations of the signal boundaries, while they are also unable to handle signals

including multiple pulses. Therefore, this new method may be part of a robust tool to estimate ultrasound signal information in both time and frequency domains. The linear (SCS) and non-linear (MB) data showed that the super-resolved frequency detection may lead to differentiating their echo signals and classify them into one of the two types successfully even with small sample sizes.

The SCS responses result in a similar number of frequency components (10 ± 1), narrow spectral peaks (Figs. 8(c) and 10)

1 and low standard deviations between the different spectra
2 (Tables V and VII) also seen in the transmit pulse (Fig. 7(c)),
3 while in the MB signals the number of frequency components
4 varies and their values tend to overlap (Fig. 9 and Table VI).
5 The increased spread of MB signal response invites further
6 work in this differentiation process. Unlike the SCS, and
7 despite the reproducibility of the specific spectral signature,
8 the MB sample size here is not adequate to characterize its
9 population. Thus, the characterization of a MB population
10 requires a large sample size. However, the comparison and
11 classification using the PSE affords a large number of degrees
12 of freedom such as number of spectral peaks, their values
13 and their estimation uncertainty, and the comparison of all
14 these to the transmit signal. The initial difference in these
15 statistics shown here, was attributed to both the high repro-
16 ducibility of the SCS responses as well as the variability of
17 the MB responses, and shows promise in the identification
18 of a single signal in the future. The SCS fundamental and
19 harmonic frequency pairs are due to their linear response,
20 fairly similar to those of the transmit pulse. It is not entirely
21 clear why the harmonic location is different to that of the
22 transmit (subsection III-C). Physical processes like non-linear
23 propagation, attenuation and speed of sound variations may
24 play a role and this merits further investigation.

25
26 The large variability in the MB responses (Fig. 10) may
27 be attributed to their variable physical behaviour. The varying
28 state of resonance due to the variable MB size distributions
29 in addition to the dispersion of shell mechanical properties
30 (not all MBs of the same size behave the same) [39], may
31 provide adequate explanation. While the experimental setup
32 is well controlled, in a real ultrasound imaging situation this
33 variability may be further enhanced. First, different locations
34 in the ultrasound beam with different ultrasound field char-
35 acteristics provide exposure to different field amplitudes and
36 frequencies [40]. Second, the consecutive pulse exposure may
37 result in a varying echo evolution state [12], [13] and third,
38 the different vessel confinements *in-vivo* may also affect the
39 MB response as arteries and veins vary from micrometres to
40 millimetres in diameter [14], [41]. The comparison of the
41 fundamental and harmonic responses from MBs and SCSs
42 (Figs. 11 and 12) is a first step towards utilizing physical
43 understanding in the examination and characterization of their
44 signals, but a much larger sample size is required for broad
45 conclusions. However, the robustness of the methodology
46 suggests that all these results may help elucidate mechanisms
47 that may be possible to quantify using PSE.

48 Further, the study of single MB acoustics [11], [42] may
49 help develop new UCI signal processing with the aim to
50 enhance the MB response. The detection of MB specific
51 signatures may help in further increasing sensitivity of UCI.
52 This may operate in the context of conventional UCI where
53 large concentrations of microbubbles are injected as a bolus or
54 intravenously, with the aim to provide images of the vascular
55 bed. Specific spectral signatures may be used to further en-
56 hance those signals. It is important to note that the theoretical
57 modelling of MB physics behaviour has not been of great
58 assistance to signal processing development. Pulse modulation
59 (amplitude or phase) that is used in current ultrasound contrast

modes [43] is more successful in tissue signal cancellation than
MB echo enhancement, as its basic aim is set to differentiate
linear from non-linear scatter. This is partly due to the inability
of the FFT to resolve spectral signature and partly due to the
cumulative effect of the above ultrasound propagation factors
and MB characteristics that contribute to the echoes within an
image pixel, when large MB concentration are utilized. The
result should not be significantly different to the cumulative
effect presented in Fig. 10, which has provided 90% successful
differentiation.

The gains from super-resolved spectral analysis may be
more appropriate for single MB processing that is currently
the subject of the newly emerging field of super-resolution
UCI [44], [45]. The method draws from the localization
microscopy and shows potential for an order of magnitude
improvement in spatial resolution. It deals with detecting and
localizing single MBs, and subsequently tracking them in the
vascular bed. Conventional ultrasound transmissions utilize
pulses that are short in order to maximize spatial resolution
at the expense of frequency resolution. So far these methods
are mainly image-based, and may benefit from the technique
presented here which has been shown to work well with short
duration raw signals. The wide range of MB responses stated
above and the ability of the spectral analysis method here to
provide high sensitivity information on each individual echo
may be beneficial to super-resolution UCI as: (a) the location
of the MB pulse can be found accurately and automatically,
(b) the MB pulses can be robustly differentiated from linear
signals and noise, (c) signal processing may be deployed to
adaptively enhance the individual characteristics of each MB
and (d) each MB may be recognized thus enabling the identifi-
cation of the next MB pulse location as a result of consecutive
ultrasound exposures, which will improve the identification
of their path. In other areas of sensing, it is possible to
implement adaptive beamforming methods to create images
of improved quality [46]–[48] that will work as an adjunct to
the above. This is a developing and exciting area of research
for ultrasound imaging.

The current algorithm requires further development in order
to provide amplitude, phase and noise estimation. For example,
the inclusion of amplitude may remove the ambiguity regard-
ing the definition of fundamental and harmonic frequencies
noted here by increasing the degrees of freedom of the com-
parison and thus resulting in improved signal classification.
Further, the capability for pulse localization and separation
will be thoroughly characterized and the dependence of the
robustness of the technique to the pulse energy, bandwidth and
SNR will be understood. The optimization of the algorithm
needs to be performed using real diagnostic ultrasound imag-
ing conditions, where the transmit pulse might not available
and only the image/signal data can inform this process. Also,
conventionally ultrasound transmissions utilize pulses that are
as short as possible in order to ensure maximization of spatial
resolution. This reduces the available energy and widens
the bandwidth in the received signals. Single MB imaging
that deploys highly sensitive spectral analysis may afford
longer pulse transmission without loss of spatial resolution
as localization methods are more dependant on the SNR and

less in the pulse duration.

VI. CONCLUSION

This paper presented a novel estimation system for echo signals from linear (solid copper spheres) and non-linear (contrast microbubbles) ultrasound scatter. The parametric model system provided the spectral and temporal parameter estimation simultaneously and automatically within the Bayesian framework. As the posterior density function cannot be solved in a closed form and the dimension of the parameters changes, a reversible jump MCMC algorithm was adopted to give the accurate estimation automatically. To speed up the convergence, a non-parametric coarse estimation for both time and frequency domains was incorporated. The results displayed precise pulse localization compared to that achieved using non-parametric methods that may provide a miscalculation of the change-points of a pulse. In addition, the parametric estimation method provided super-resolved frequency spectra that resulted in increased number of detected frequencies compared to the number of peaks detected by Fourier Transform based methods. Further, the spectra of echo signals from linear and non-linear scatter provided different characteristics, which may be deployed to advance UCI signal processing in the future.

REFERENCES

- [1] Q. Wen, S. Wan, Z. Liu, S. Xu, H. Wang, and B. Yang, "Ultrasound contrast agents and ultrasound molecular imaging," *J. Nanosci. Nanotechnol.*, vol. 14, no. 1, pp. 190–209, Jan. 2014.
- [2] B. A. Kaufmann, K. Wei, and J. R. Lindner, "Contrast echocardiography," *Curr. Probl. Cardiol.*, vol. 32, no. 2, pp. 51–96, 2007.
- [3] E. Quai, "Microbubble ultrasound contrast agents: an update," *Eur. Radiol.*, vol. 17, no. 8, pp. 1995–2008, 2007.
- [4] P. A. Dijkmans, P. Knaapen, G. T. J. Sieswerda, E. Aiazian, C. A. Visser, A. A. Lammertsma, F. C. Visser, and O. Kamp, "Quantification of myocardial perfusion using intravenous myocardial contrast echocardiography in healthy volunteers: Comparison with positron emission tomography," *J. Am. Soc. Echocardiogr.*, vol. 19, no. 3, pp. 285–293, 2006.
- [5] M.-X. Tang, H. Mulvana, T. Gauthier, A. K. P. Lim, D. O. Cosgrove, R. J. Eckersley, and E. Stride, "Quantitative contrast-enhanced ultrasound imaging: a review of sources of variability," *Interface Focus*, vol. 1, no. 4, pp. 520–539, 2011.
- [6] C. A. Miller, J. H. Naish, M. P. Ainslie, C. Tonge, D. Tout, P. Arumugam, A. Banerji, R. M. Egde, D. Clark, P. Weale, C. D. Steadman, G. P. McCann, S. G. Ray, G. J. Parker, and M. Schmitt, "Voxel-wise quantification of myocardial blood flow with cardiovascular magnetic resonance: effect of variations in methodology and validation with positron emission tomography," *J. Cardiovasc. Mag. Res.*, vol. 16, no. 11, pp. 1–15, Jan. 2014.
- [7] F. Pathan and T. H. Marwick, "Myocardial perfusion imaging using contrast echocardiography," *Prog. Cardiovasc. Dis.*, vol. 57, no. 6, pp. 632–643, May 2015.
- [8] F. Conversano, R. Franchini, A. Lay-Ekuakille, and S. Casciaro, "In vitro evaluation and theoretical modeling of the dissolution behavior of a microbubble contrast agent for ultrasound imaging," *IEEE Sensors Journal*, vol. 12, no. 3, pp. 496–503, Mar. 2012.
- [9] K. Christensen-Jeffries, S. Harput, J. Brown, P. N. T. Wells, P. Aljabar, C. Dunsby, M. X. Tang, and R. J. Eckersley, "Microbubble axial localization errors in ultrasound super-resolution imaging," *IEEE Trans. Ultrason., Ferroelectr., Freq. Control*, vol. 64, no. 11, pp. 1644–1654, 2017.
- [10] V. Sboros, "A review of single microbubble acoustics," in *Proc. of 20th Int. Cong. on Acous., ICA*, Aug 2010, pp. 1–5.
- [11] D. H. Thomas, M. B. Butler, T. Anderson, R. Steel, S. D. Pye, M. Poland, T. Brock-Fisher, W. N. McDicken, and V. Sboros, "Single microbubble response using pulse sequences: initial results," *Ultr. Med. Biol.*, vol. 35, no. 1, pp. 112–119, 2009.
- [12] D. H. Thomas, M. Butler, T. Anderson, M. Emmer, H. Vos, M. Borden, E. Stride, N. de Jong, and V. Sboros, "The 'quasi-stable' lipid shelled microbubble in response to consecutive ultrasound pulses," *Appl. Phys. Lett.*, vol. 101, no. 7, p. 071601, 2012.
- [13] D. H. Thomas, M. Butler, N. Pelekasis, T. Anderson, E. Stride, and V. Sboros, "The acoustic signature of decaying resonant phospholipid microbubbles," *Phys. Med. Biol.*, vol. 58, no. 3, pp. 589–599, 2013.
- [14] D. H. Thomas, V. Sboros, M. Emmer, H. Vos, and N. D. Jong, "Microbubble oscillations in capillary tubes," *IEEE Trans. Ultrason., Ferroelectr., Freq. Control*, vol. 60, no. 1, pp. 105–114, Jan. 2013.
- [15] A. Needles, M. Arditi, N. G. Rognin, J. Mehi, T. Coulthard, C. Bilan-Tracey, E. Gaud, P. Frinking, D. Hirson, and F. S. Foster, "Nonlinear contrast imaging with an array-based micro-ultrasound system," *Ultr. Med. Biol.*, vol. 36, no. 12, pp. 2097–2106, 2010.
- [16] S. Hilgenfeldt, D. Lohse, and M. Zomack, "Sound scattering and localized heat deposition of pulse-driven microbubbles," *J. Acoust. Soc. Am.*, vol. 107, no. 6, pp. 3530–3539, 2000.
- [17] E. Stride and N. Saffari, "Microbubble ultrasound contrast agents: a review," *Proceedings of the Institution of Mechanical Engineers, Part H: Journal of Engineering in Medicine*, vol. 217, pp. 429–447, 2003.
- [18] A. Greco, M. Mancini, S. Gargiulo, M. Gramanzini, P. P. Claudio, A. Brunetti, and M. Salvatore, "Ultrasound biomicroscopy in small animal research: applications in molecular and preclinical imaging," *J. Biomed. Biotechnol.*, vol. 2012, p. 519238, 2012.
- [19] P. Hoskins, K. Martin, and A. Thrush, *Diagnostic ultrasound: Physics and equipment*, 2nd ed. Cambridge University Press, 2010.
- [20] Y. Yan, J. R. Hopgood, and V. Sboros, "Analysis of echo signal from single ultrasound contrast microbubble using a reversible jump mcmc algorithm," in *Proc. IEEE Eng. in Med. and Biol. Soc.*, 2007, pp. 1273–1276.
- [21] —, "Bayesian spectral estimation applied to echo signals from nonlinear ultrasound scatterers," *EURASIP Journal on Advances in Sig. Proc.*, vol. 2011, p. 146175, Nov. 2010.
- [22] K. Diamantis, M. A. Dhali, G. Gibson, Y. Yan, J. R. Hopgood, and V. Sboros, "Super-resolution spectral analysis for ultrasound scatter characterization," in *Proc. IEEE Int. Conf. Acous., Speech, Sig. Pro. (ICASSP)*, 2016, pp. 903–907.
- [23] J.-H. Chang, N. S. Kim, and S. K. Mitra, "Voice activity detection based on multiple statistical models," *IEEE Trans. on Sig. Proc.*, vol. 54, no. 6, pp. 1965–1976, 2006.
- [24] Y. D. Cho, K. Al-Naimi, and A. Kondoz, "Improved statistical voice activity detection based on a smoothed statistical likelihood ratio," in *Proc. IEEE Int. Conf. Acous., Speech, Sig. Pro. (ICASSP)*, 2001, pp. 737–740.
- [25] J. Sohn, N. S. Kim, and W. Sung, "A statistical model-based voice activity detection," *IEEE Sig. Proc. Lett.*, vol. 6, no. 1, pp. 1–3, 1999.
- [26] M. Wacker and H. Witte, "Time-frequency techniques in biomedical signal analysis: a tutorial review of similarities and differences," *Methods. Inf. Med.*, vol. 52, no. 4, pp. 279–296, May 2013.
- [27] Y. Yan, J. R. Hopgood, and V. Sboros, "A novel estimation system for multiple pulse echo signals from ultrasound contrast microbubbles," in *Proc. IEEE Int. Conf. Acous., Speech, Sig. Pro. (ICASSP)*, 2008, pp. 601–604.
- [28] V. Sboros, S. D. Pye, C. A. MacDonald, J. Gomatam, C. M. Moran, and W. N. McDicken, "Absolute measurement of ultrasonic backscatter from single microbubbles," *Ultr. Med. Biol.*, vol. 31, no. 8, pp. 1063–1072, 2005.
- [29] E. L. Madsen, G. R. Frank, and F. Dong, "Liquid or solid ultrasonically tissue-mimicking materials with very low scatter," *Ultr. Med. Biol.*, vol. 24, no. 4, pp. 535–542, 1998.
- [30] A. Xander, A. M. Verbeek, L. A. F. Ledoux, P. J. Brands, and A. P. G. Hoeks, "Baseband velocity estimation for second-harmonic signals exploiting the invariance of the doppler equation," *IEEE Trans. Biomed. Eng.*, vol. 45, no. 10, pp. 1217–1226, 1998.
- [31] X. Lu, R. Liu, J. Liu, and S. Liang, "Removal of noise by wavelet method to generate high quality temporal data of terrestrial MODIS products," *Photogrammetric Eng. and Remote Sensing*, vol. 73, no. 10, 2007.
- [32] G. Soloperto, F. Conversano, A. Greco, E. Casciaro, R. Franchini, and S. Casciaro, "Advanced spectral analyses for real-time automatic echographic tissue-typing of simulated tumor masses at different compression stages," *IEEE Trans. Ultrason., Ferroelectr., Freq. Control*, vol. 59, no. 12, pp. 2692–2701, Dec. 2012.
- [33] D. G. Manolakis, V. K. Ingle, and S. M. Kogon, *Statistical and adaptive signal processing: spectral estimation, signal modeling, adaptive filtering and array processing*. McGrawHill Companies, Inc., 2000.

[34] P. Stoica and Y. Selen, "Model order selection: A review of information criterion rules," *IEEE Sig. Proc. Mag.*, vol. 21, no. 4, pp. 36–47, 2004.

[35] P. Gregory, *Bayesian inference and maximum entropy methods in science and engineering*. Kluwer academic publishers, 2001.

[36] G. A. F. Seber, *Multivariate Observations*. Hoboken, NJ: John Wiley & Sons, 1984.

[37] M. S. Lawrence, *Digital spectral analysis*. Englewood Cliffs, NJ: Prentice-Hall, 1987.

[38] A. W. Bowman and A. Azzalini, *Applied Smoothing Techniques for Data Analysis*. New York, USA: Oxford University Press, 1997.

[39] D. H. Thomas, P. Looney, R. Steel, N. Pelekasis, W. N. McDicken, T. Anderson, and V. Sboros, "Acoustic detection of microbubble resonance," *Appl. Phys. Lett.*, vol. 94, no. 24, p. 243902, 2009.

[40] V. Sboros, "Response of contrast agents to ultrasound," *Advanced Drug Delivery Reviews*, vol. 60, no. 10, pp. 1117–1136, 2008.

[41] M. B. Butler, D. H. Thomas, N. Silva, S. D. Pye, and V. Sboros, "Acoustic detection of microbubble resonance," *Appl. Phys. Lett.*, vol. 99, no. 19, p. 193702, 2011.

[42] D. H. Thomas, M. B. Butler, A. Dermitzakis, T. Anderson, W. N. McDicken, and V. Sboros, "The acoustic scatter from single bisphere microbubbles," *Ultr. Med. Biol.*, vol. 36, no. 11, pp. 1884–1892, 2010.

[43] E. Stride and N. Saffari, "Microbubble ultrasound contrast agents: a review," *Proc. Inst. Mech. Eng. H.*, vol. 217, no. 6, pp. 429–447, 2003.

[44] M. A. O'Reilly, R. M. Jones, and K. Hynynen, "Three-dimensional transcranial ultrasound imaging of microbubble clouds using a sparse hemispherical array," *IEEE Trans. Biom. Eng.*, vol. 61, no. 4, pp. 1285–1294, 2014.

[45] K. Christensen-Jeffries, R. J. Browning, M. X. Tang, C. Dunsby, and R. J. Eckersley, "In vivo acoustic super-resolution and super-resolved velocity mapping using microbubbles," *IEEE Trans. Medical Imaging*, vol. 34, no. 2, pp. 433–440, Feb. 2015.

[46] K. Diamantis, I. H. Voxen, A. H. Greenaway, T. Anderson, J. A. Jensen, and V. Sboros, "A comparison between temporal and subband minimum variance adaptive beamforming," in *Proc. SPIE Med. Imag.*, vol. 90400L, Mar. 2014. [Online]. Available: [10.1117/12.2043602](https://doi.org/10.1117/12.2043602).

[47] K. Diamantis, A. Greenaway, T. Anderson, J. Jensen, P. Dalgarno, and V. Sboros, "Super-resolution axial localization of ultrasound scatter using multi-focal imaging," *IEEE Trans. Biomed. Eng.*, vol. PP, no. 99, pp. 1–1, 2017.

[48] K. Diamantis, A. Greenaway, T. Anderson, J. A. Jensen, and V. Sboros, "Experimental performance assessment of the sub-band minimum variance beamformer for ultrasound imaging," *Ultrasonics*, vol. 79, pp. 87–95, 2017.



Konstantinos Diamantis was born in Athens, Greece. He received the diploma in electrical and computer engineering, and the M.Sc. degree in biomedical engineering both from the University of Patras, Greece, in 2009 and 2011 respectively, and the Ph.D. degree in medical imaging from Heriot-Watt (HW) University, Edinburgh, UK, in 2016. He is currently a post-doctoral research associate with the Institute of Biological Chemistry, Biophysics and Bioengineering (IB3), Heriot-Watt University, Edinburgh, UK. His research interests include array signal processing, adaptive beamforming, statistical signal processing, super-resolution ultrasound imaging, and medical image analysis.



Aris Dermitzakis was born in Athens, Greece. He received the diploma in electrical and computer engineering, the M.Sc. degree in biomedical engineering, and the Ph.D. degree in the field of brain gliomas simulation for use in X-ray imaging techniques all from the University of Patras, Greece, in 2007, 2009 and 2014 respectively. He is currently a post-doctoral research associate with the Biomedical Technology Unit, Department of Medical Physics, University of Patras, Greece. He is a member of the Auditing Committee of the Hellenic Society of Biomedical Engineering, and his research interests include X-ray imaging simulation, brain modelling and imaging, image processing, ultrasound contrast agents, and ultrasound imaging.



James R. Hopgood (M'02) is a Senior Lecturer in the Institute for Digital Communications, within the School of Engineering, at the University of Edinburgh, Scotland. He received the M.A. (Hons), M.Eng. degree from the University of Cambridge in electrical and information sciences in 1997, and a Ph.D. in July 2001 in statistical signal processing from the same University. He was then a Research Fellow for three years at Queens' College Cambridge and the Signal Processing Laboratory in the Cambridge University Engineering Department. James joined the University of Edinburgh as a Lecturer in April 2004, and then Senior Lecturer in 2012. Since September 2011, he is Editor-in-Chief for the IET Journal of Signal Processing. His research expertise include model-based Bayesian inference, speech and audio signal processing in adverse acoustic environments, including blind dereverberation and multi-target acoustic source localization and tracking, single channel signal separation, audio-visual fusion, medical imaging, and blind image deconvolution.



Vassilis Sboros was born in Volos, Greece in 1968. He graduated from the University of Athens with Physics degree in 1993, and from the University of Aberdeen with an M.Sc. in medical physics in 1994. His Ph.D. on ultrasound contrast imaging at the University of Edinburgh was completed in 1999. The jobs that followed investigated the physics of microbubbles and the engineering of imaging them. His current interests expand to clinical and preclinical ultrasound imaging. He has published over 50 peer reviewed papers.